

Sleep Homeostasis and Cortical Synchronization: I. Modeling the Effects of Synaptic Strength on Sleep Slow Waves

Steve K. Esser, BS^{1,2*}; Sean L. Hill, PhD^{1*}; Giulio Tononi, MD, PhD¹

¹Department of Psychiatry and ²Neuroscience Training Program, University of Wisconsin, Madison, WI; *Both authors contributed equally to this work

Study Objectives: Sleep slow-wave activity (SWA, electroencephalogram [EEG] power between 0.5 and 4.0 Hz) is homeostatically regulated, increasing with wakefulness and declining with sleep. Sleep SWA is thought to reflect sleep need, but the mechanisms of its homeostatic regulation remain unknown. Based on a recent hypothesis, we sought to determine whether a decrease in cortical synaptic strength can account for changes in sleep SWA.

Design: A large-scale computer model of the sleeping thalamocortical system was used to reproduce in detail the cortical slow oscillations underlying EEG slow waves.

Setting: N/A.

Patients or Participants: N/A.

Interventions: Simulated reductions in the strength of corticocortical synapses.

Measurements and Results: Decreased synaptic strength led to (1) decreased single cell membrane potential oscillations and reduced network synchronization, (2) decreased rate of neural recruitment

and decruitment, and (3) emergence of local clusters of synchronized activity. These changes were reflected in the local EEG as (1) decreased incidence of high-amplitude slow waves, (2) decreased wave slope, and (3) increased number of multipeak waves. Spectral analysis confirmed that these changes were associated with a decrease in SWA.

Conclusions: A decrease in cortical synaptic strength is sufficient to account for changes in sleep SWA and is accompanied by characteristic changes in slow-wave parameters. Experimental results from rat cortical depth recordings and human high-density EEG show similar changes in slow-wave parameters with decreasing SWA, suggesting that the underlying mechanism may indeed be a net decrease in synaptic strength.

Keywords: Sleep homeostasis, synaptic plasticity, slow oscillation, SWA, computer model

Citation: Esser SK; Hill SL; Tononi G. Sleep homeostasis and cortical synchronization: I. Modeling the effects of synaptic strength on sleep slow waves. *SLEEP* 2007;30(12):1617-1630.

SLOW WAVES ARE A PROMINENT FEATURE OF NON-RAPID EYE MOVEMENT (NREM) SLEEP THAT CAN BE OBSERVED IN THE ELECTROENCEPHALOGRAPH (EEG) and local field potentials (LFP). Slow-wave activity (SWA, EEG power 0.5-4.0 Hz) provides a reliable indicator of sleep need, as it increases as a function of prior waking and declines during sleep.¹⁻³ Although the homeostatic regulation of SWA is suggestive of a restorative function of sleep, the underlying mechanisms remain unknown.

Different mechanisms can be conceived that might lead to a progressive decline in SWA during sleep, such as an increase in the level of arousal-promoting neuromodulators or a reduction of accumulated metabolites (e.g., adenosine). A recent proposal suggests that the level of SWA may reflect the strength of corticocortical synapses and that a progressive reduction in synaptic strength during sleep would be associated with a corresponding decrease in SWA.^{4,5} Mechanistically, stronger cortical connections would produce stronger network synchronization and thus a higher level of SWA, whereas weaker connections would reduce network synchronization and thereby SWA. Connections would become, on average, stronger at the end of a waking day due to synaptic potentiation associated with learning and would

weaken during sleep due to sleep-dependent synaptic depression, as suggested by molecular and other evidence.^{4,5} Supporting the hypothesis, procedures associated with synaptic potentiation and depression in local cortical areas lead to corresponding changes in sleep SWA. For example, sleep SWA increases over right parietal cortex after a visuomotor learning task⁶ and decreases over the right sensorimotor cortex after immobilization of the left arm.⁷

In this paper, we employed a large-scale computer model of the cat thalamocortical system to investigate in detail the relationship between synaptic strength and SWA. The model incorporates key aspects of the neuroanatomic organization of visual thalamocortical circuits, including more than 65,000 integrate-and-fire neurons organized into multiple cortical, thalamic, and reticular areas, and produces physiologically realistic sleep activity patterns.⁸ Specifically, due to the interaction between several intrinsic and synaptic currents, simulated neurons undergo slow oscillations at around 1 Hz between depolarized periods of activity (up states) and hyperpolarized periods of silence (down states), as observed in intracellular recordings in vivo.^{9,10} These single-cell oscillations are synchronized by corticocortical connections and produce realistic slow waves in the calculated LFP.

On the basis of this model, we examined the dynamics of single-cell oscillations, cortical synchronization, and LFP slow waves under conditions with a high or low strength of corticocortical connections. We show here that a reduction in cortical synaptic strength leads to a decrease in sleep SWA, a decreased incidence of large-amplitude slow waves, a decrease in their slope, and an increase in the number of multipeak waves. In 2 companion papers, we tested the predictions of the model by examining how slow waves change between early-sleep and late-sleep conditions using LFP recordings in rats¹¹ and high-density EEG recordings in humans.¹²

Disclosure Statement

This was not an industry supported study. The authors have indicated no financial conflicts of interest.

Submitted for publication December, 2006

Accepted for publication September, 2007

Address correspondence to: Giulio Tononi, Department of Psychiatry, University of Wisconsin-Madison, 6001 Research Park Blvd, Madison, WI 53719; E-mail: gtononi@wisc.edu

METHODS

Large-Scale Thalamocortical Model of NREM Sleep

The large-scale model used here is described in detail in a previously published paper.⁸ In what follows, we briefly describe the principles used to construct and scale the simulated cortical and thalamic regions, the layout of the various connection pathways within and among these regions, and the implementation of cellular and synaptic properties. We then describe the sources of spontaneous activity and the procedures for the collection and analysis of data. In previous work, we demonstrated that this model is able to produce realistic slow waves and provided a detailed analysis of the role that the various model components play in slow-wave generation.⁸

Regional Organization

Primary Cortical Area

The model (Figure 1) is organized in regions and pathways comprising a primary and a secondary area of visual cortex, 2 corresponding regions of the dorsal thalamus, and 2 regions of the reticular thalamic nucleus. The primary visual area (Vp) represents a restricted portion of cat striate cortex (area 17) and contains units with small receptive fields that are selective for oriented segments. The simulated cortex is divided into 3 layers with different patterns of afferent, efferent, and local connectivity corresponding to supragranular layers (L2-3), infragranular layers (L5-6), and layer 4 (L4).

The model area Vp corresponds to approximately 0.8 cm² of striate cortical surface and spans a monocular patch of 8×8 degrees in the parafoveal visual field. Each topographic location (topographic element) in the model cortex is considered to correspond to a cortical column, which is represented by 9 model neurons (2 excitatory and 1 inhibitory for each of the 3 layers). The topographic elements in Vp are organized in maps of 40×40 elements and are orientation selective. Orientation selectivity is achieved via the convergence of afferents from an oriented rectangular region in Tp onto individual cortical cells in L4 and L5-6. The subdivision of the modeled cortical areas in elements spanning all layers reflects the developmental, anatomic, and physiologic evidence for a basic columnar organization of neocortex.¹³

Secondary Cortical Area

The secondary visual area (Vs) corresponds to an extrastriate area located along the ventral occipitotemporal pathway. In the model, Vs is based on some general properties associated with extrastriate areas (e.g., an enlargement of receptive fields) and with termination patterns of “forward” and “backward” corticocortical projections.^{14, 15} Vs contains neurons that are selective for vertical lines, horizontal lines, or line crossings, organized in a coarse topographic map. For each of its 3 selectivities, Vs has a map of 30×30 elements (for a total of 24,300 model neurons), as compared to the 40×40 (totalling 28,800 model neurons) elements in Vp.

Thalamic Sectors

Each element of the dorsal thalamus (Tp) contains 2 modeled neurons that correspond respectively to an X-relay cell and to an

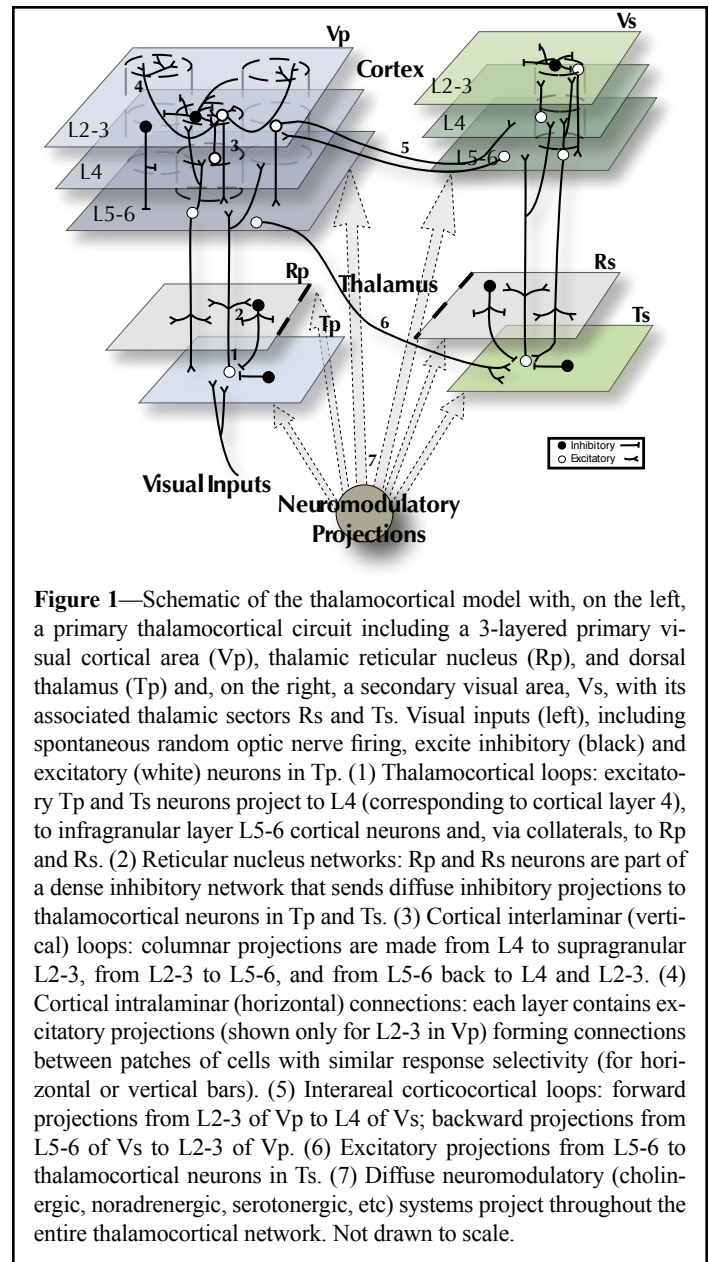


Figure 1—Schematic of the thalamocortical model with, on the left, a primary thalamocortical circuit including a 3-layered primary visual cortical area (Vp), thalamic reticular nucleus (Rp), and dorsal thalamus (Tp) and, on the right, a secondary visual area, Vs, with its associated thalamic sectors Rs and Ts. Visual inputs (left), including spontaneous random optic nerve firing, excite inhibitory (black) and excitatory (white) neurons in Tp. (1) Thalamocortical loops: excitatory Tp and Ts neurons project to L4 (corresponding to cortical layer 4), to infragranular layer L5-6 cortical neurons and, via collaterals, to Rp and Rs. (2) Reticular nucleus networks: Rp and Rs neurons are part of a dense inhibitory network that sends diffuse inhibitory projections to thalamocortical neurons in Tp and Ts. (3) Cortical interlaminar (vertical) loops: columnar projections are made from L4 to supragranular L2-3, from L2-3 to L5-6, and from L5-6 back to L4 and L2-3. (4) Cortical intralaminar (horizontal) connections: each layer contains excitatory projections (shown only for L2-3 in Vp) forming connections between patches of cells with similar response selectivity (for horizontal or vertical bars). (5) Interareal corticocortical loops: forward projections from L2-3 of Vp to L4 of Vs; backward projections from L5-6 of Vs to L2-3 of Vp. (6) Excitatory projections from L5-6 to thalamocortical neurons in Ts. (7) Diffuse neuromodulatory (cholinergic, noradrenergic, serotonergic, etc) systems project throughout the entire thalamocortical network. Not drawn to scale.

inhibitory interneuron. For simplicity of implementation, only the ON portion of thalamic receptive fields is modeled. The secondary thalamic map (Ts) has 30×30 elements, and its visuotopic arrangement has a much lower spatial resolution than Tp (40×40). Two sectors of the reticular nucleus, primary perigeniculate (Rp) and secondary higher-order (Rs), are modeled, respectively, as a 40×40 and a 30×30 map of inhibitory neurons.

Connectivity

In constructing the model, special emphasis was put on the incorporation of realistic network properties, such as the spread and relative proportions of the various sets of connections composing the intraregional and interregional thalamocortical circuitry. Contacts from individual arbors in the target area are made probabilistically according to Gaussian spatial density profiles. The proportion of synapses from different sources was used as a constraint in the parameterization of the various density profiles, as detailed in Table 1 of Hill and Tononi.⁸ The ratio of excitatory/inhibitory (~80%/20%) synapses observed in vivo is maintained in the distri-

bution of model connections. Books by Sherman and Guillery¹⁶ and White and Keller¹⁷ were particularly helpful in the development of this model. The model included a variety of excitatory cortical connections, including interlaminar connections that couple neurons vertically through the cortical depth, intralaminar connections that horizontally connected neurons with similar orientation preference, and feedforward and feedback interareal connections connecting Vp and Vs. Intralaminar GABAergic connections provided inhibition in the local cortical area. Cortex and the thalamic and reticular areas were connected by a variety of corticothalamic and thalamocortical connections. Connections within thalamus delivered local excitation and inhibition, and connections from the reticular nucleus to the thalamus provided a strong inhibition to thalamic neurons.

Transmission of signals within and across cortical areas occurs through several successive stages, including axonal conduction, synaptic delays, and postsynaptic potential generation. Each of these stages is associated with delays in the transmission of a signal, which were taken into account when establishing transmission delays between specific cortical populations, as described in Table 1 of Hill and Tononi.⁸

Model Neurons

Both excitatory and inhibitory neurons are modeled as single-compartment spiking neurons incorporating Hodgkin–Huxley-style currents. In order to model the contributions of key intrinsic currents, while preserving the computational efficiency of integrate-and-fire neurons that is necessary when computing a large-scale network, we devised a simplification of the fast spiking currents (I_{Na} and I_K). Model neurons thus behave like a hybrid between traditional integrate-and-fire neurons and full-fledged Hodgkin–Huxley neurons.

The change in subthreshold membrane potential V for each neuron is as follows:

$$\frac{dV}{dt} = (-g_{NaL}(V - E_{Na}) - g_{KL}(V - E_K) - I_{syn} - I_{int}) / \tau_m,$$

where the conductances and reversal potentials for the sodium leak ($g_{NaL} = 0.2$; $E_{Na} = 30$ mV) and potassium leak ($g_{KL} = 1.95$; $E_K = -90$ mV) are the primary determinants of the resting membrane potential. Conductance units are dimensionless due to the fact that the neurons do not have a defined area or volume. The membrane time constants, τ_m , were consistent with experimental data for excitatory and inhibitory cells (see Table 2 of Hill and Tononi⁸). Two main categories of input currents contribute to the membrane potential: synaptic input (I_{syn}) and intrinsic currents (I_{int}), which are described below.

When the membrane potential V exceeded a threshold, a spike was generated. The fast sodium and potassium currents were modeled as pulses of current, which greatly reduced their computational requirements. The cells were considered to enter a refractory period following each spike.

Synaptic Channels

The synaptic input, I_{syn} , is the sum of all synaptic channel currents:

$$I_{syn} = \sum_{ij} g_j^{(i)} (V - E_j)$$

Simulated synaptic channels provide voltage-dependent (NMDA-like) and voltage-independent (AMPA-like) excitation, as well as fast ($GABA_A$ -like) and slow ($GABA_B$ -like) inhibition. The conductance g_j for each afferent i , on each channel j , specifies the amplitude and time course of the postsynaptic potentials (PSPs). The reversal potential for each channel E_j determines whether a current is inhibitory or excitatory.

Short-Term Synaptic Depression

There is substantial evidence that the rapid plasticity of excitatory and inhibitory synaptic responses is dominated by short-term depression and caused by the depletion of presynaptic pools of readily releasable neurotransmitter vesicles.¹⁸ In the model, short-term depression of both excitatory and inhibitory connections was based on a simple vesicle pool model.¹⁹ Short-term synaptic depression was modeled by scaling the peak conductance of a given synaptic channel by the size of the corresponding presynaptic pool of synaptic “vesicles,” which depleted with neuronal firing and recovered with time.

Intrinsic Ion Channel Properties of Thalamic and Cortical Neurons

Ion channel currents influence intrinsic firing properties of thalamic and cortical neurons, and are modeled by incorporating Hodgkin–Huxley-style currents into the single-compartment model described above. The specific equations, models, and distributions of the channels are described elsewhere.⁸ I_h is a noninactivating hyperpolarization-activated cation current that underlies a depolarizing “pacemaker” potential observed in many cells throughout the brain, including the thalamus and the cortex.^{20, 21} I_T is a low-threshold fast-activating calcium current that underlies the generation of bursts in the thalamus and reticular nucleus.^{21, 22} Persistent sodium current $I_{Na(p)}$ activates quickly near the resting potential and is considered persistent because it inactivates very slowly (on the order of seconds). A Na^+ or Ca^{2+} -activated K^+ current appears to play an important role in the termination of the depolarized phase of the slow oscillation. This current was modeled as a depolarization activated potassium current, I_{DK} .^{23, 24}

Influence of Diffuse Neuromodulatory Systems

Under physiologic conditions, ascending neuromodulatory projections modulate the mode of firing in the thalamocortical system. Ascending neuromodulatory projections from several brainstem nuclei and the basal forebrain activate cholinergic, noradrenergic, serotonergic, histaminergic, and glutamatergic metabotropic receptors. These receptors modulate various cellular conductances that influence the overall level of depolarization on which the sleep-wake cycle critically depends.²⁵ The various actions of neuromodulators are modeled as simultaneous changes of the conductances for I_{KL} , I_h , I_{DK} , $I_{Na(p)}$ and AMPA synapses of the cortex, thalamus, and reticular nucleus.

Spontaneous Activity: Optic Nerve Firing and Minis

The primary source of noise in the model was random spontaneous optic tract firing (45 spikes/s) modeled as 1600 separate Poisson processes connected to Tp. This random activity perco-

lated throughout the network, producing irregular spontaneous activity in all layers of the model.

In addition, we modeled “minis,” the spontaneous release of neurotransmitter quanta,²⁶ as low-amplitude PSPs (mean = 0.5 ± 0.25 mV), consistent with experimental observations.²⁷ The mean frequency of these Poisson-distributed synaptic minis was set to 2 Hz (total for an individual cell).

Data Gathering and Analysis

Membrane potentials and synaptic currents were recorded for all units during 60 seconds at 1-KHz sampling for each condition, starting from identical initial conditions. The LFP depth recording is believed to primarily reflect a summation of local postsynaptic currents in pyramidal cells according to the equation:

$$V_{ext} = \frac{R_e}{4\pi} \sum_j \frac{I_j}{r_j}$$

where V_{ext} is the extracellular potential, R_e (230 Ω cm) is the extracellular resistivity, I_j is the postsynaptic current, and r_j is the distance from synaptic activity I_j to the recording site.²⁸ For all cells, we set r_j to the mean distance between all neurons and the center of the network (0.35 cm) so as not to bias the recording toward specific cells. The activity in the network (Figure 2A-C) was reflected by this LFP recording (Figure 2D) with opposite polarity, such that a negative deflection in the LFP reflected a period of depolarization in the network. It should be noted that the LFP was smaller in amplitude than typical *in vivo* recordings due to the sparse representation of neurons in the model. The EEG is believed to reflect the summation of postsynaptic currents in cortical pyramidal cells but with reversed polarity.²⁹ An approximate EEG was therefore derived by summing the postsynaptic currents in all cortical excitatory cells in primary visual cortex and reversing the resulting signal's polarity (Figure 2E). Both the LFP (Figure 2D) and EEG (Figure 2E) were band-pass filtered (0.5-30 Hz, stopband edge frequencies 0.1-80 Hz, stopband minimal attenuation 10 dB) using Chebyshev Type II filter design.

Detection of individual slow waves was performed on the signal after subtracting the mean value of the signal (to center the signal around zero) and band-pass filtering (0.5-2 Hz, stopband edge frequencies 0.1-10 Hz, stopband minimal attenuation 10 dB) using Chebyshev Type II filter design. The filter settings were optimized visually based on the shape of the spectrum to achieve the best resolution in terms of wave shape, with the least contamination by fast activity. LFP slow waves were defined as positive deflections of the signal between 2 consecutive negative-going peaks below the zero-crossing (detections based on zero crossings gave similar results). Subsequently, peak-to-peak amplitude (measured from the largest magnitude negative peak to the positive peak), wave slopes for the first wave segment (linear slope from the first negative peak to the positive peak), and second-wave segment (linear slope from the positive peak to the second negative peak), instantaneous wave slope at the steepest point of the first and second wave segment, and the number of positive peaks between 2 consecutive zero crossings were computed for all individual, filtered waves. The software package MATLAB (The Math Works, Inc., Natick, MA) was used for signal and data analysis.

To measure network synchronization at slow-wave frequencies, recordings of membrane potentials had spikes cropped at -53

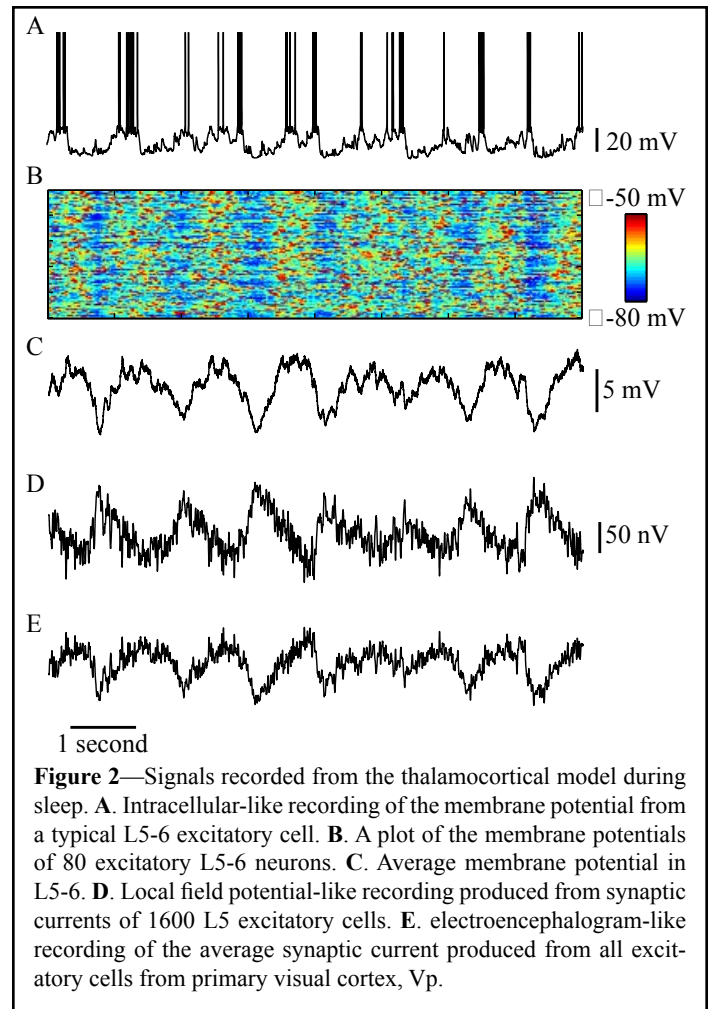


Figure 2—Signals recorded from the thalamocortical model during sleep. **A.** Intracellular-like recording of the membrane potential from a typical L5-6 excitatory cell. **B.** A plot of the membrane potentials of 80 excitatory L5-6 neurons. **C.** Average membrane potential in L5-6. **D.** Local field potential-like recording produced from synaptic currents of 1600 L5 excitatory cells. **E.** electroencephalogram-like recording of the average synaptic current produced from all excitatory cells from primary visual cortex, Vp.

mV and were band-pass filtered (0.5-2 Hz, stopband edge frequencies 0.1-10 Hz, stopband minimal attenuation 10 dB) using Chebyshev Type II filter design. Phase angle was then calculated by defining, for each cell's filtered membrane potential, $x(t)$, an analytic signal $Z_x(t) = x(t) + i\tilde{x}(t) = A(t)e^{i\Phi(t)}$, where $\Phi(t)$ is the signal phase and $\tilde{x}(t)$ is the Hilbert transform of $x(t)$ ³⁰

$$\tilde{x}(t) = \frac{1}{\pi} P.V. \int_{-\infty}^{\infty} \frac{x(\tau)}{t - \tau} d\tau$$

(P.V. means the integral is taken in the sense of the Cauchy principal value). A phase synchronization index for a population of neurons was calculated as 1 minus the circular variance of the cell phases³¹ according to the equation:

$$PSI(t) = \sqrt{\left(\frac{1}{n} \sum_{i=1}^n \cos \phi(t)_i \right)^2 + \left(\frac{1}{n} \sum_{i=1}^n \sin \phi(t)_i \right)^2}$$

where $PSI(t)$ is the phase synchronization index at time t , $\Phi_i(t)$ is the phase of cell i at time t , and n is the number of neurons. This produces a phase synchronization index ranging from 0 to 1, with 0 indicating no phase synchronization and 1 indicating perfect phase synchronization. To test for possible confounds, this analysis was also performed without first clipping spikes, which produced similar results.

To measure changes in activity during slow waves, each wave was divided into 11 equal-length sections before the wave peak

and 11 equal-length sections after the wave peak. For the 21 time points between these sections, we examined how each cell's average membrane potential during the previous section changed, compared with the cell's average membrane potential during the subsequent section. If a cell's average membrane potential changed from below -65 mV to above -65 mV, it was considered to be *recruited*, whereas if it changed from above -70 mV to below -70 mV, it was considered to be *decruted*. These thresholds were chosen based on the bimodal distribution of neural membrane potentials. Thus, recruitment was used as a measure of cells entering the active up state, whereas decruitment was a measure of cells entering the silent down state during a given slow wave. For each time segment, the average LFP was also calculated. LFP slope across each time point was then calculated as the difference between these average values divided by the length of the corresponding time segment.

Small-Scale Model of Coupled Oscillators

To demonstrate the effect of decreasing coupling strength on synchronization, we simulated activity in a small-scale model under conditions of decreasing synaptic strength. The model consisted of 50 single-compartment, intrinsically oscillating neurons incorporating voltage-dependent currents described according to Hodgkin-Huxley kinetics³²

$$C_m \frac{dV}{dt} = -g_L(V - E_L) - I^{\text{int}} - I^{\text{syn}}$$

with membrane capacitance, $C_m = 1 \mu\text{F}/\text{cm}^2$, leak conductance, $g_L = 0.03 \text{ mS}/\text{cm}^2$, leak reversal potential, $E_L = -80 \text{ mV}$, I^{int} representing intrinsic currents, and I^{syn} representing synaptic current. Each neuron was simulated with a surface area of $1000 \mu\text{m}^2$.

Intrinsic currents included fast sodium current and fast potassium current, described in Hodgkin and Huxley.³² Two additional intrinsic currents were created to produce an approximately 1-Hz oscillation in the neurons, I_{dep} , which was depolarizing from rest, and I_{hyp} , which was hyperpolarizing from rest. For I_{dep} and I_{hyp} , the current was modeled as $I = \bar{g}m(V - E)$, where the conductance was $\bar{g} = 15.0 \text{ mS}/\text{cm}^2$ and the steady states values of the gating variables m and h were $m_{\infty}(V) = 1/(1 + \exp((-65 - V)/5))$ and $h_{\infty}(V) = 1/(1 + \exp((65 + V)/5))$. For I_{dep} ,

$$\frac{dm}{dt} = (m_{\infty}(V) - m)/10, \quad \frac{dh}{dt} = (m_{\infty}(V) - m)/\tau_{\text{cycle}}$$

and the reversal potential was $E = -40 \text{ mV}$. For I_{hyp} ,

$$\frac{dm}{dt} = (m_{\infty}(V) - m)/\tau_{\text{cycle}}, \quad \frac{dh}{dt} = (m_{\infty}(V) - m)/10$$

and the reversal potential was $E = -85 \text{ mV}$. The cycle time constant, τ_{cycle} was randomly set for each cell between 400 and 600 milliseconds, which produced membrane potential oscillations of approximately 0.8 to 1.2 Hz. Synaptic currents were modeled as AMPA-like currents, using equations previously described.⁸ Baseline synaptic conductance was set to $0.064 \text{ mS}/\text{cm}^2$ so as to produce oscillations in the average membrane potential comparable to those we observed in the large-scale model.

The 50 cells were arranged in a 1-dimensional circular array (such that the right side and left side of the array connected to

each other). Each cell connected to the 5 nearest cells to either side. Simulations were performed using this small-scale model with synaptic strength set to 100%, 25%, 6.25%, and 1.56% of baseline levels.

RESULTS

It is well known that the synchronization of coupled oscillators is heavily influenced by the strength of the coupling.³³ Thus, in principle, one should expect that the synchrony of neurons oscillating in a network should decrease with reduced synaptic strength. Indeed, in a network of 50 intrinsically oscillating Hodgkin-Huxley neurons,³² we found that network synchronization decreased with reduced synaptic strength (Figure 3). However, a more realistic, large-scale model such as the one described above, is needed to examine in detail how a decrease in synaptic strength affects the generation of cortical slow waves at multiple levels, from ionic mechanisms to network synchronization and LFP dynamics. To this end, we used the large-scale model described in the Methods in 2 conditions. The model (Figure 1) was first run to simulate sleep with synaptic strength sufficient to produce clearly defined intracellular slow oscillations for the high-synaptic-strength condition (Figure 2). These synchronized oscillations appear in the LFP as high-amplitude slow waves. To model the possible effects of synaptic downscaling, the strength of excitatory intralaminar, interlaminar, and corticocortical connections was scaled down to 85% of the baseline value for the low-synaptic-strength condition. Specifically, g_{peak} in the channel conductance equation was reduced to 85% of its value in the high-synaptic-strength condition, leading to a proportional reduction of postsynaptic currents to both excitatory and inhibitory targets. Other than the change in synaptic strength, these 2 simulations began with identical initial conditions (i.e., the same initial membrane potentials and channel conductances in all cells) and used all the same model parameters and connections. Runs in both conditions were performed for 45 seconds of simulated time, which provided the dataset analyzed below. Our results did not change in any substantial way when simulations were performed using different random-number seeds to produce other sets of network connections and initial conditions. Furthermore, using a range of connection strength values (i.e., 80%-90% of the high-synaptic-strength condition) for the low-synaptic-strength condition produced results similar to those presented here.

SWA and Network Synchronization Decrease with Reduced Synaptic Strength

In the high-synaptic-strength condition, the model neurons exhibited periods of asynchronous activity as well as frequent, clearly defined, and well-synchronized up and down states of the slow oscillation, reflected as high-amplitude waves in the LFP (Figure 4A,C). By contrast, in the low-synaptic-strength condition, the model neurons exhibited a decreased number of clearly defined high-amplitude slow oscillations, visible in the LFP as a marked decrease in the amplitude and regularity of oscillatory activity (Figure 4B,D). The autocorrelation of the LFPs (Figure 4E) showed that the network activity was more synchronized in the high-synaptic-strength condition than in the low-synaptic-strength condition (the peak of the autocorrelation in the low-synaptic-strength condition was 60% of the peak in the high-synaptic-strength condition).

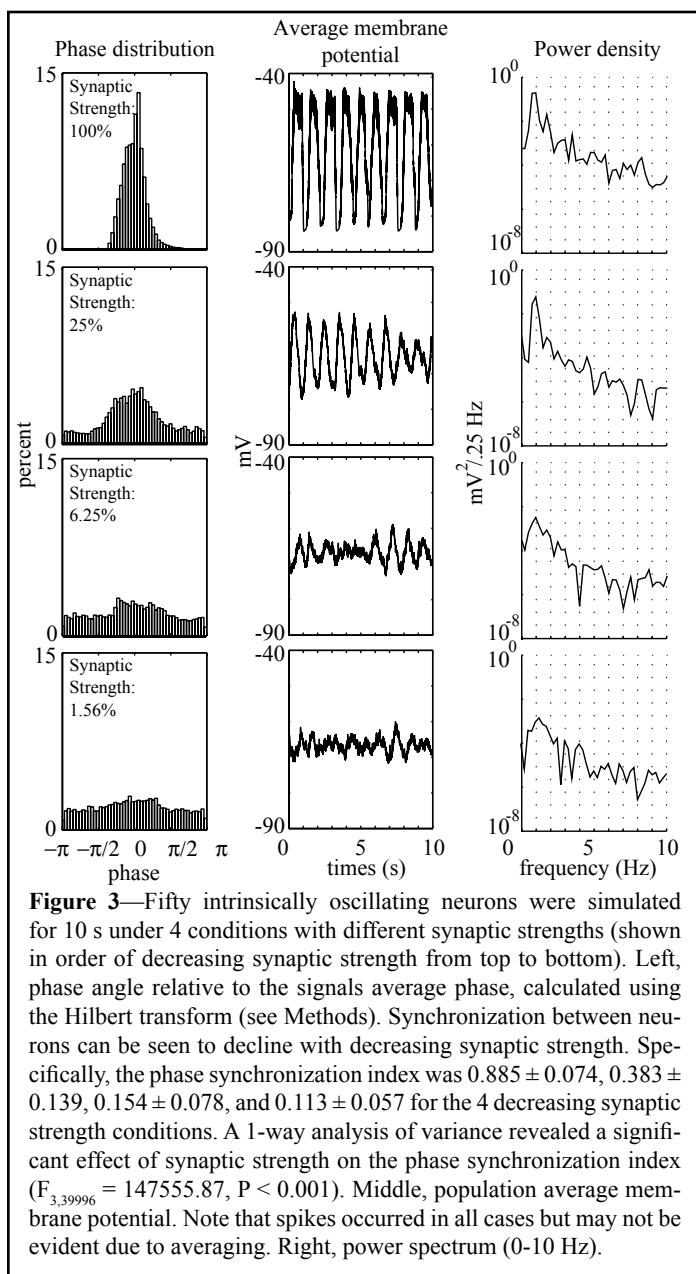


Figure 3—Fifty intrinsically oscillating neurons were simulated for 10 s under 4 conditions with different synaptic strengths (shown in order of decreasing synaptic strength from top to bottom). Left, phase angle relative to the signals average phase, calculated using the Hilbert transform (see Methods). Synchronization between neurons can be seen to decline with decreasing synaptic strength. Specifically, the phase synchronization index was 0.885 ± 0.074 , 0.383 ± 0.139 , 0.154 ± 0.078 , and 0.113 ± 0.057 for the 4 decreasing synaptic strength conditions. A 1-way analysis of variance revealed a significant effect of synaptic strength on the phase synchronization index ($F_{3,39996} = 147555.87$, $P < 0.001$). Middle, population average membrane potential. Note that spikes occurred in all cases but may not be evident due to averaging. Right, power spectrum (0–10 Hz).

tic-strength condition).

To investigate the effects of decreased synaptic strength on SWA, we subdivided the LFP into 11 four-second epochs and computed their power spectra. There was a marked decrease in SWA (Figure 5) in the low-synaptic-strength condition compared with the high-synaptic-strength condition. Specifically, the peak in the power spectra declined from 0.410 ± 0.279 nV²/25 Hz (mean \pm SD) in the high-synaptic-strength condition to 0.085 ± 0.098 nV²/25 Hz in the low-synaptic-strength condition ($P < 0.05$, unpaired t-test, $n = 11, 11$). To statistically analyze the peak frequency in these power spectra, we excluded epochs that contributed little to the power of the peaks (those with maximum power less than one third of the size of the peak in the respective power spectrum) and determined the frequency of the peak power in each of the remaining epochs. We found that the average peak frequency in these epochs shifted from 1.00 ± 0.00 Hz in the high-synaptic-strength condition to 0.85 ± 0.09 Hz in the low-synaptic-strength condition ($P < 0.05$, unpaired t-test, $n = 8, 7$).

Slow Wave Morphology Changes as a Function of Synaptic Strength

We then examined how individual slow waves changed as a function of synaptic strength by measuring their amplitude, their slope, and the number of multipeak waves. In order to compare these 3 parameters with those measured in companion physiologic experiments performed in rats¹¹ and humans,¹² the simulated LFP was low-pass filtered and the component waves were extracted using techniques similar to those in the companion papers (see Methods and Figure 4F). This was performed for both the high- and low-synaptic-strength conditions (Figure 4). The total number of waves extracted was slightly greater in the low-synaptic-strength condition (number of waves in a 45-second time span: high = 44, low = 53).

Reduced Synaptic Strength Leads to a Decrease in the Incidence of Slow Waves with High Amplitude

The reduction in synaptic strength was associated with a decrease in the incidence of waves with high amplitude and an increase in the incidence of waves with low amplitude (Figure 6A). The peak amplitude shifted from 58.12 ± 22.51 nV for the high-synaptic-strength condition to 25.10 ± 16.04 nV for the low-synaptic-strength condition ($P < 0.001$, unpaired t-test, $n = 44, 53$).

Reduced Synaptic Strength Leads to a Decrease in the Slope of the Slow Waves

This decrease in amplitude was accompanied by a decrease in the slope of the first and second segment of the slow waves (Figure 6B). The mean slope of the first segment decreased significantly ($P < 0.001$, unpaired t-test, $n = 44, 53$) from 127.69 ± 57.73 nV/second in the high-synaptic-strength condition to 57.68 ± 29.34 nV/second in the low-synaptic-strength condition. The mean second-segment slope decreased in magnitude significantly ($P < 0.001$, unpaired t-test, $n = 44, 53$) from -96.46 ± 39.35 nV/second in the high-synaptic-strength condition to -51.41 ± 28.49 nV/second in the low-synaptic-strength condition.

When we measured the maximum instantaneous slope (Figure 6C), we found that the average maximum slope of the first segment decreased significantly from 217.50 ± 107.17 nV/second in the high-synaptic-strength condition to 118.06 ± 60.78 nV/second in the low-synaptic-strength condition ($P < 0.001$, unpaired t-test, $n = 44, 53$). The average maximum slope of the second segment decreased in magnitude significantly from -176.71 ± 58.50 nV/second in the high-synaptic-strength condition to -110.29 ± 41.48 nV/second in the low-synaptic-strength condition ($P < 0.001$, unpaired t-test, $n = 44, 53$).

Reduced Synaptic Strength Leads to an Increase in the Number of Multipeak Waves

As the wave amplitude and slopes decreased, the emergence of multipeak waves became increasingly pronounced (Figure 6D). The number of peaks ranged from 1 to 5 per wave. The percentage of waves with multiple peaks increased from 25.0% for the high-synaptic-strength condition to 35.8% for the low-synaptic-strength condition.

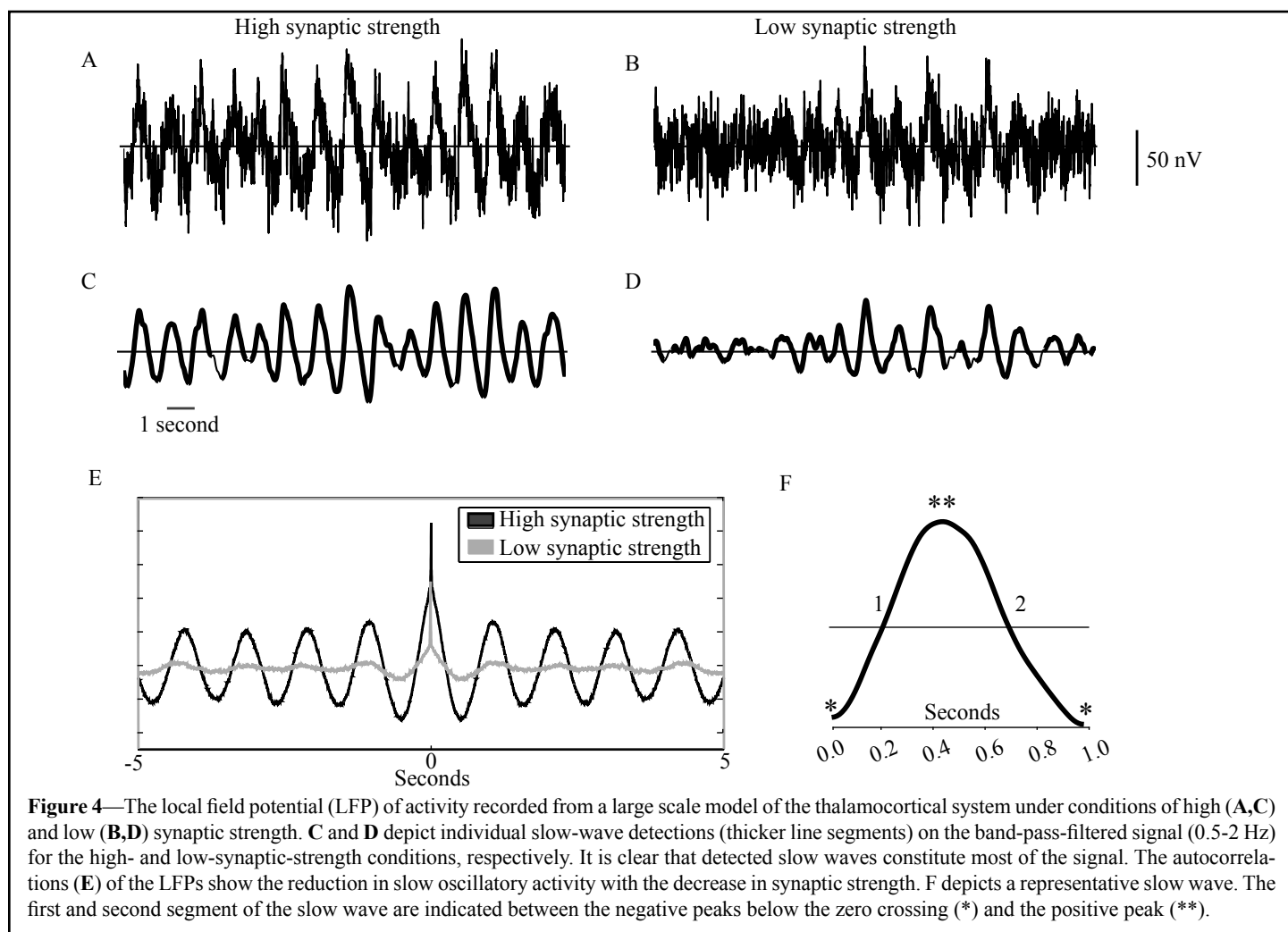


Figure 4—The local field potential (LFP) of activity recorded from a large scale model of the thalamocortical system under conditions of high (A,C) and low (B,D) synaptic strength. C and D depict individual slow-wave detections (thicker line segments) on the band-pass-filtered signal (0.5-2 Hz) for the high- and low-synaptic-strength conditions, respectively. It is clear that detected slow waves constitute most of the signal. The autocorrelations (E) of the LFPs show the reduction in slow oscillatory activity with the decrease in synaptic strength. F depicts a representative slow wave. The first and second segment of the slow wave are indicated between the negative peaks below the zero crossing (*) and the positive peak (**).

Mechanisms Responsible for the Changes in Slow Waves Associated with Decreased Synaptic Strength

To examine the cellular mechanisms responsible for the changes in the LFP associated with decreased synaptic strength, we examined the intracellular membrane potential and firing rates of 1600 excitatory neurons from L5 to L6. These measures were chosen to provide insight into the neuronal activity underlying the generation of the synaptic currents collectively recorded in the LFP. Throughout the slow wave, activity extending through the column (including supragranular L2-3 and L4) was similar to that observed in L5-6 (Figure 7A).

A Decreased Incidence of Slow Waves with High Amplitude is the Result of Reduced Single-Cell Membrane Potential Oscillations and Decreased Network Synchronization

In concert with the slow wave observed at the network level, at the cellular level individual neurons undergo alternating silent periods of hyperpolarization and active periods of depolarization (Figure 2). The level of postsynaptic currents, and thus the amplitude of the slow waves observed in the LFP (Figure 7B), is determined by this underlying neuronal activity. To understand how this neuronal activity changes under conditions of low synaptic strength, we measured the amplitude and synchrony of single-cell membrane-potential oscillations as well as the number of cells recruited in each slow wave. In a perfectly synchronous network,

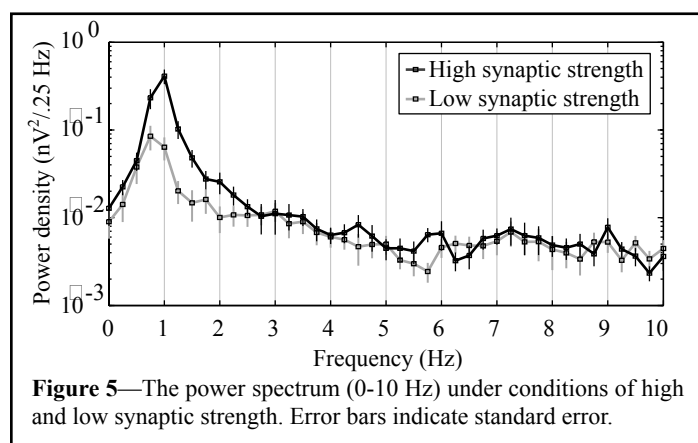


Figure 5—The power spectrum (0-10 Hz) under conditions of high and low synaptic strength. Error bars indicate standard error.

reducing the amplitude of the membrane potential oscillations in each cell will decrease the average level of firing in the network. On the other hand, if the amplitude of single-cell oscillations is held fixed, then decreasing the synchrony of the network will result in more cells with oscillations that are out of phase with each other (i.e., some cells are in the up state while other cells are in the down state). The activity of cells in opposite phases of the slow oscillation will cancel each other out, resulting in a reduction of the slow-wave amplitude. We found that the amplitude of single-cell oscillations decreased and that the single-cell oscillations were more out of phase with one another under conditions of low synaptic strength. Specifically, decreased synaptic strength

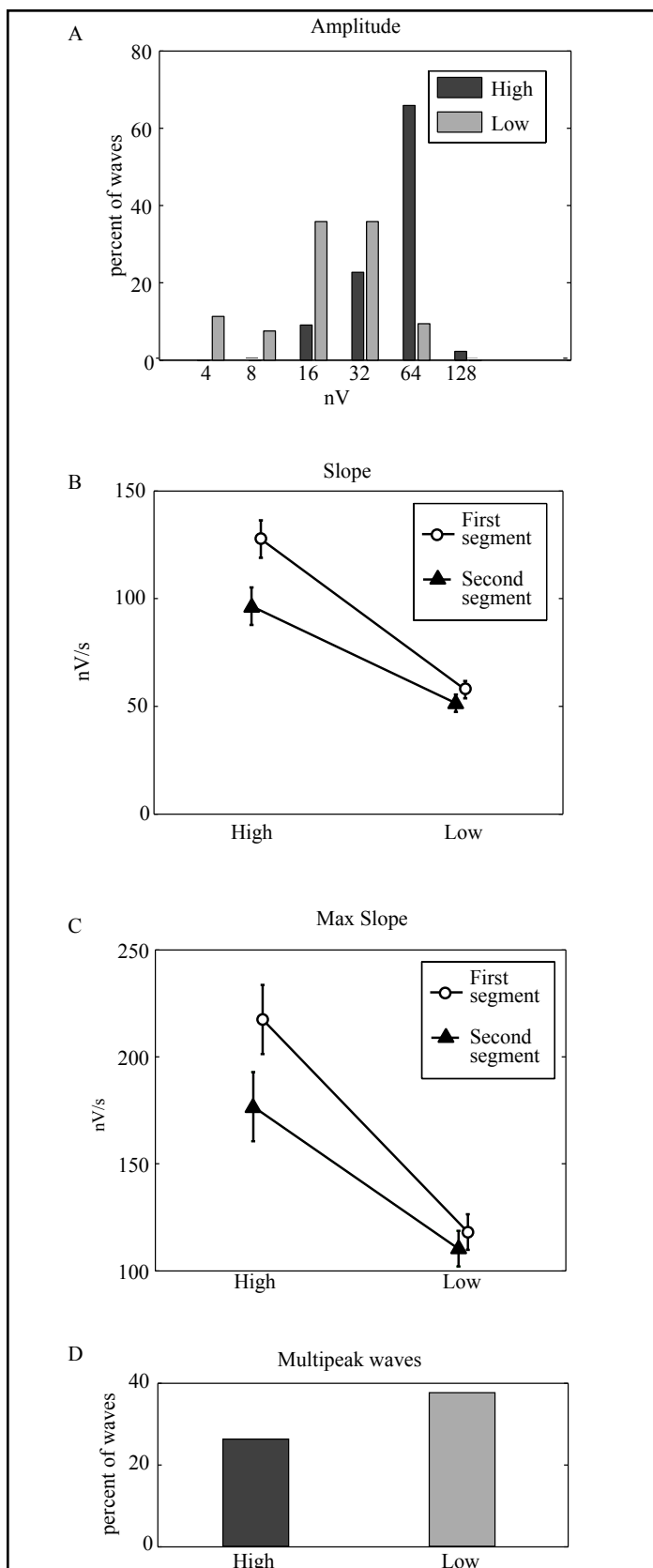


Figure 6—Changes in slow-wave parameters as synaptic strength decreases. **A.** Distribution of slow-wave amplitude, shown with bin width increasing in a logarithmic fashion. **B.** Absolute value of the slope of the first and second segment of the slow waves (error bars depict standard error). **C.** Absolute value of the maximum instantaneous slope of the first and second segment of the slow waves (error bars depict standard error). In both slope figures, the absolute value of the slope is shown for ease of comparison. **D.** Number of multippeak waves.

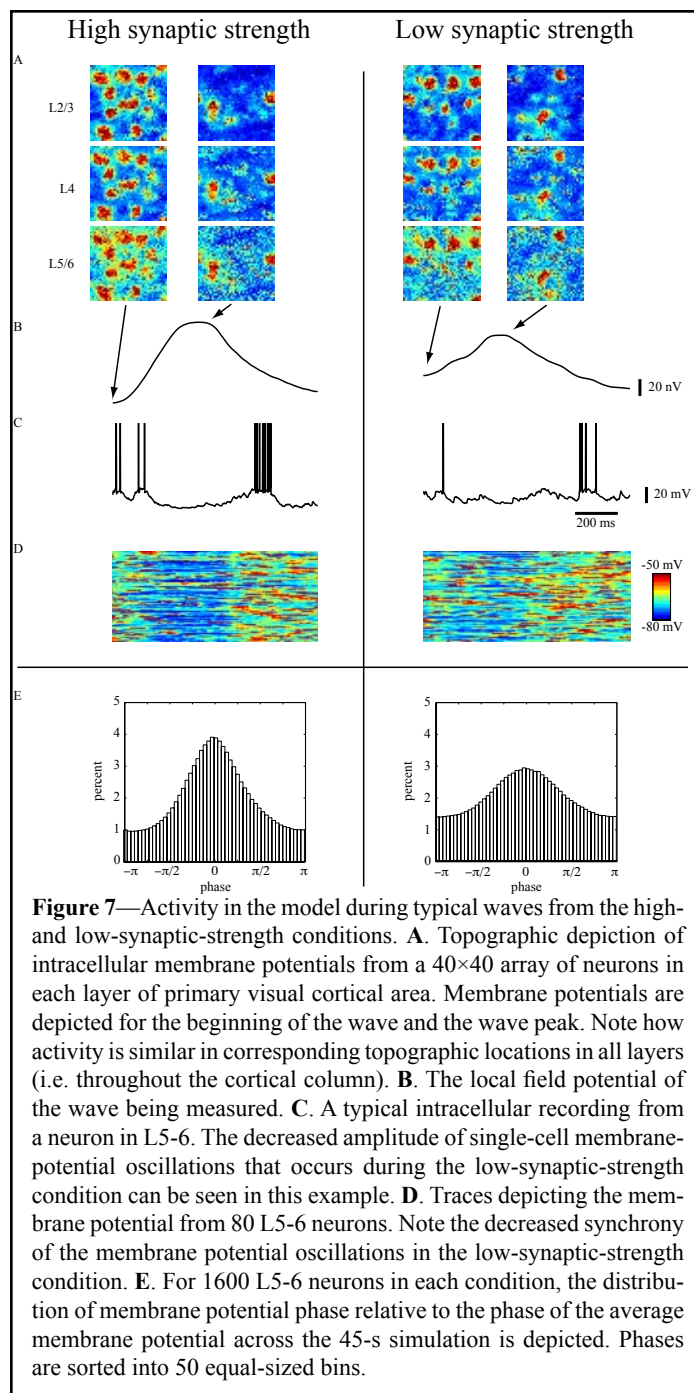


Figure 7—Activity in the model during typical waves from the high- and low-synaptic-strength conditions. **A.** Topographic depiction of intracellular membrane potentials from a 40×40 array of neurons in each layer of primary visual cortical area. Membrane potentials are depicted for the beginning of the wave and the wave peak. Note how activity is similar in corresponding topographic locations in all layers (i.e. throughout the cortical column). **B.** The local field potential of the wave being measured. **C.** A typical intracellular recording from a neuron in L5-6. The decreased amplitude of single-cell membrane-potential oscillations that occurs during the low-synaptic-strength condition can be seen in this example. **D.** Traces depicting the membrane potential from 80 L5-6 neurons. Note the decreased synchrony of the membrane potential oscillations in the low-synaptic-strength condition. **E.** For 1600 L5-6 neurons in each condition, the distribution of membrane potential phase relative to the phase of the average membrane potential across the 45-s simulation is depicted. Phases are sorted into 50 equal-sized bins.

resulted in smaller excitatory postsynaptic potentials, leading to a reduced amplitude of single-cell membrane-potential oscillations (Figure 7C). For each cell, the amplitude of single-cell membrane-potential oscillations was measured by first centering the single-cell membrane potential on the population mean. The average rectified value of the resulting mean-centered trace was used as the amplitude of each cell's membrane potential oscillations. This measure of membrane-potential oscillation was significantly reduced in the low-synaptic-strength condition (5.64 ± 0.72 mV) compared with the high-synaptic-strength condition (6.05 ± 0.79 mV) ($P < 0.001$, unpaired t-test, $n = 1600, 1600$).

The reduction in synaptic strength also resulted in reduced coupling between individual neurons and led to a reduction in the synchronization of single cell oscillations (Figure 7D,E). Specifically, the phase synchronization index, calculated for all time points in the 45-second period from each condition, had a

significantly lower average value ($P < 0.001$; unpaired t-test) in the low-synaptic-strength condition (0.20 ± 0.11) than in the high-synaptic-strength condition (0.34 ± 0.15).

The Decreased Slope of Slow Waves Resulted from a Reduced Rate of Neuronal Decruitment and Recruitment

Decreasing synaptic strength resulted in a lower level of decruitment from the preceding depolarized wave phase. The rate at which cells were decruited was measured at 21 time points over the duration of each slow wave, as described in the Methods (Figure 8A). The average rate of decruitment was $5.51\% \pm 1.93\%$ in the high-synaptic-strength condition and $4.52\% \pm 1.30\%$ in the low-synaptic-strength condition ($P < 0.001$, unpaired t-test, $n = 44, 53$). The rate of decruitment reflects the rate at which individual cells leave the depolarized phase of the slow oscillation, become hyperpolarized, and stop firing. This suggests that higher rates of decruitment should lead to a steeper slope of the LFP when the network is entering a hyperpolarized state. Indeed, we found that, during the first segment of the slow wave, the rate of decruitment at each time point and the slope across the corresponding time point were correlated ($r = 0.38$, $P < 0.001$).

Decreasing synaptic strength in the model also resulted in a change in how cells are recruited during each slow wave (Figure 8B). The average rate of recruitment was $5.88\% \pm 1.83\%$ in the high-synaptic-strength condition and $4.71\% \pm 0.96\%$ in the low-synaptic-strength condition ($P < 0.001$, unpaired t-test, $n = 44, 53$). The rate of recruitment is a direct reflection of the rate at which individual cells leave the hyperpolarized phase of the slow oscillation, become depolarized, and produce spikes. This suggests that higher rates of recruitment should lead to a steeper slope of the LFP when the network is entering a depolarized state. Indeed, we found that during the second segment of the slow wave, the rate of recruitment at each time point and the slope across the corresponding time point were correlated ($r = 0.29$, $P < 0.001$).

Multiple Peaks in the Slow Waves Resulted from a Decreased Rate of Decruitment and Reduced Synchronization Leading to the Emergence of Local Clusters of Activity

Decreasing synaptic strength and the subsequent decrease in the rate of decruitment and reduction in network synchrony resulted in the emergence of local clusters of activity. Due to their intrinsic neuronal currents, each column (modeled as a vertically oriented group of 9 neurons) has the propensity to enter the hyperpolarized down state independently of other cells in the network. In the high-synaptic-strength condition, the increased coupling between neurons, with the subsequent high rate of decruitment and elevated network synchrony, meant that neurons across the network tended to enter the hyperpolarized down state in a single contiguous group. Thus, single groups of cells entering the down state were manifested in the LFP as single-peaked waves (Figure 9, left). By contrast, the reduced rate of decruitment and lower network synchrony in the low-synaptic-strength condition meant that the population of neurons was more likely to fragment into multiple local clusters of activity. These local clusters of activity appeared in the LFP as waves with multiple peaks (Figure 9, right). As shown in Figure 6D, the number of these waves with more than 1 peak increased as synaptic strength declined.

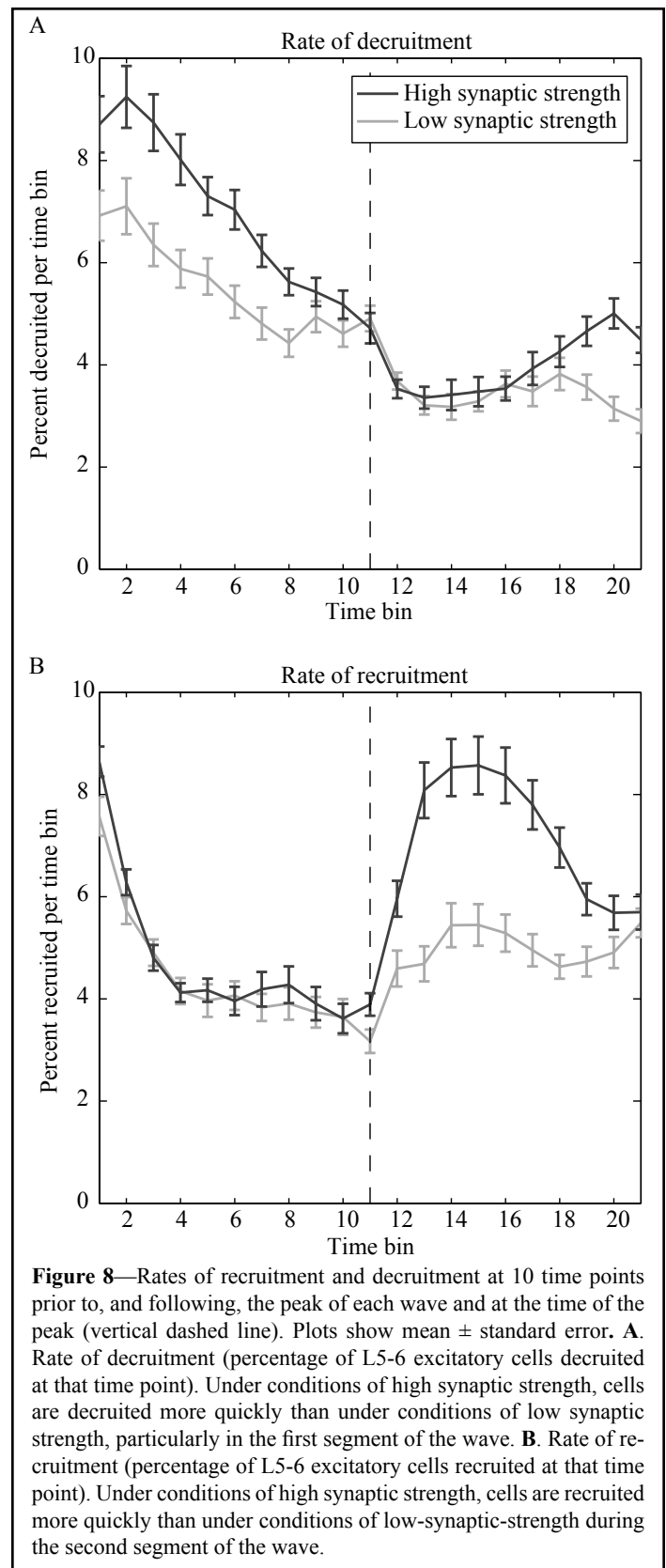
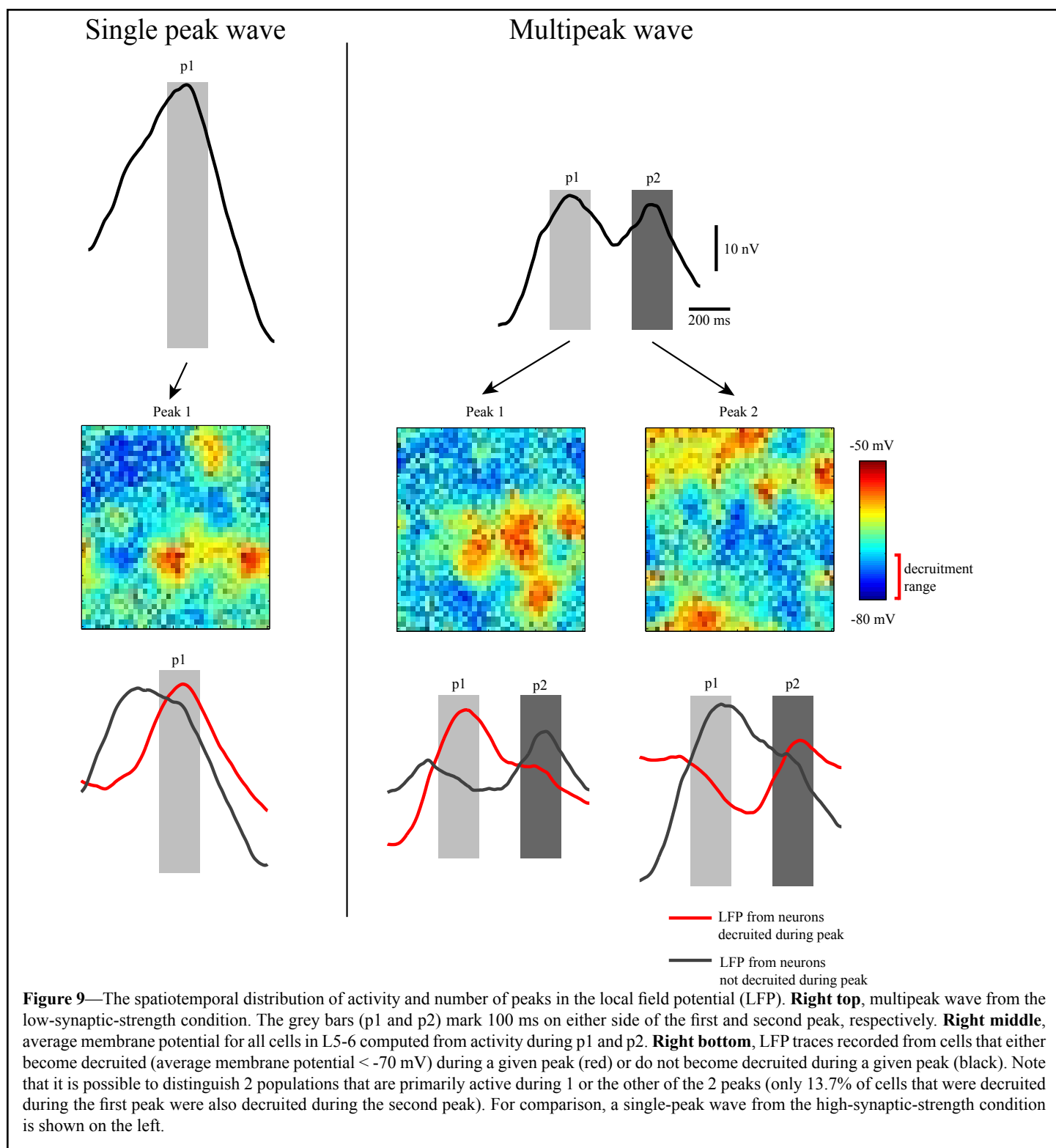


Figure 8—Rates of recruitment and decruitment at 10 time points prior to, and following, the peak of each wave and at the time of the peak (vertical dashed line). Plots show mean \pm standard error. **A.** Rate of decruitment (percentage of L5-6 excitatory cells decruited at that time point). Under conditions of high synaptic strength, cells are decruited more quickly than under conditions of low synaptic strength, particularly in the first segment of the wave. **B.** Rate of recruitment (percentage of L5-6 excitatory cells recruited at that time point). Under conditions of high synaptic strength, cells are recruited more quickly than under conditions of low-synaptic-strength during the second segment of the wave.

Comparing the Effect on Slow Waves of Changes in Synaptic Strength and Arousal-Promoting Neuromodulators

In the model, the transition from wakefulness to sleep is mediated by a decrease in the levels of arousal-promoting neuromodulators, which produces a change in several intrinsic and synaptic conductances (see⁸ for details). To investigate how such changes



affect slow waves, we held synaptic strength constant at 100% of baseline levels and simulated sleep with increased levels of arousal-promoting neuromodulators. We defined the normal sleep and waking level of arousal-promoting neuromodulators as 0% and 100%, respectively. We then gradually increased the sleep level to 15%. This manipulation produced an LFP that visually resembles the one produced in the low-synaptic-strength condition (Figure 10A,B). Thus, an increase in the level of arousal-promoting neuromodulators without changes in synaptic strength can, in principle, result in changes to slow waves that appear

SLEEP, Vol. 30, No. 12, 2007

similar to those produced by a decrease in synaptic strength. To further investigate these changes, we then equated slow waves for amplitude (within 5 nV) between the low-synaptic-strength condition and the increased-neuromodulation condition (Figure 10C) and compared the slopes of these wave pairs for 2 minutes of simulated data in each condition (Figure 10D). Note that we extended our low-synaptic-strength condition simulations to 2 minutes for this comparison so that sufficient wave pairs would be generated ($n = 133$) to achieve sufficient statistical power. We found that, for waves of equal amplitude, the wave slope of the

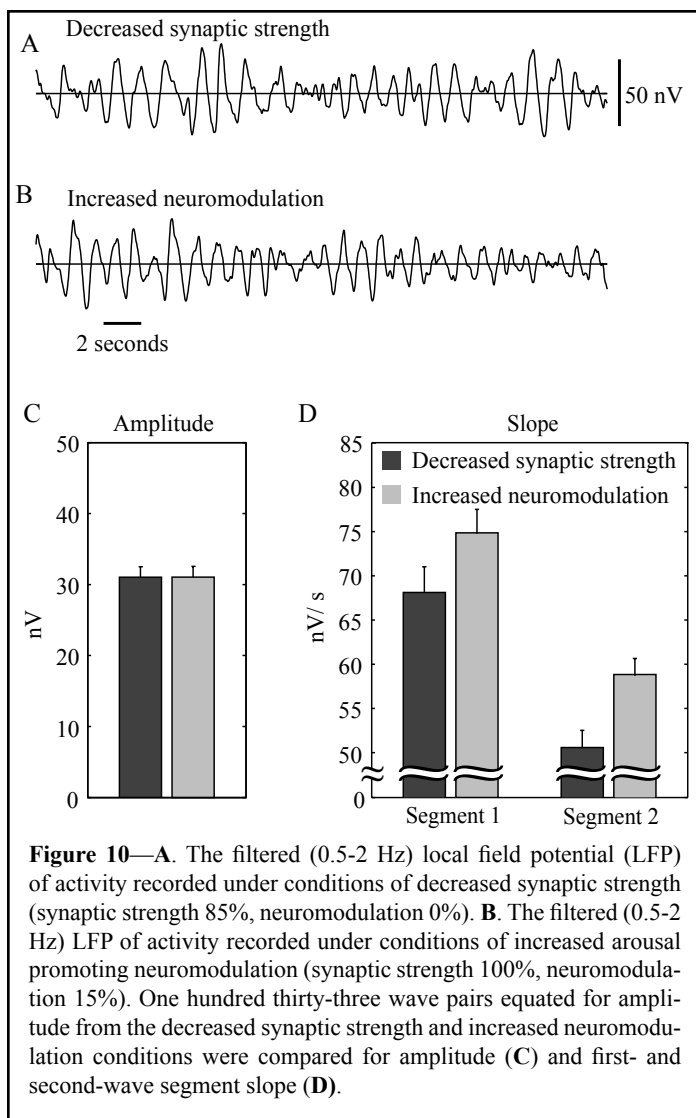


Figure 10—A. The filtered (0.5-2 Hz) local field potential (LFP) of activity recorded under conditions of decreased synaptic strength (synaptic strength 85%, neuromodulation 0%). **B.** The filtered (0.5-2 Hz) LFP of activity recorded under conditions of increased arousal promoting neuromodulation (synaptic strength 100%, neuromodulation 15%). One hundred thirty-three wave pairs equated for amplitude from the decreased synaptic strength and increased neuromodulation conditions were compared for amplitude (**C**) and first- and second-wave segment slope (**D**).

first segment was significantly lower in the decreased synaptic strength condition (68.03 ± 33.23 nV/s) compared with the increased neuromodulation condition (74.89 ± 34.89 nV/s; $P < 0.01$, paired t-test, $n = 133$). Similarly, for waves of equal amplitude, the wave slope of the first segment was also significantly lower in magnitude following a decrease in synaptic strength (-51.32 ± 22.91 nV/s), compared to an increase in arousal-promoting neuromodulators (-58.45 ± 24.22 nV/s; $P < 0.01$, paired t-test, $n = 133$). Thus, reducing synaptic strength resulted in a larger decrease of wave slope from baseline levels than increasing arousal-promoting neuromodulators.

Effects of Reducing the Synaptic Strength of Specific Cortical Connections

To examine whether changes to specific sets of synaptic connections might produce different effects than decreasing the synaptic strength of all excitatory corticocortical connections, we simulated 45 seconds of sleep with the following connection sets reduced to 85% of baseline levels: interlayer excitatory connections (Vertical 85%), intralayer excitatory connections (Horizontal 85%), thalamocortical connections (Thalamocortical 85%), corticocortical excitatory and inhibitory connections (Exc and Inh 85%), and cortical inhibitory connections (Inh 85%). These

Table 1—Wave Amplitude with All Connections at 100% Strength and with Specific Sets of Connections at 85% Strength

| Connection reduced in strength | Wave amplitude | No. |
|--------------------------------|-------------------|-----|
| All 100% | 58.12 ± 22.51 | 44 |
| Exc 85% | 25.10 ± 16.04 | 53 |
| Vertical 85% | 50.42 ± 25.18 | 41 |
| Horizontal 85% | 36.94 ± 21.16 | 48 |
| Thalamocortical 85% | 53.15 ± 29.73 | 49 |
| Exc and Inh 85% | 48.72 ± 19.73 | 44 |
| Inh 85% | 70.62 ± 35.09 | 48 |

Data are expressed as mean \pm SD. Exc refers to excitatory; Inh, inhibitory.

conditions were compared with the high (All 100%) and low-synaptic-strength (Exc 85%) conditions considered above. For each of these conditions, mean wave amplitude and standard deviation are listed in Table 1. A 1-way analysis of variance revealed a significant difference between the conditions ($F_{6,320} = 13.86$, $P < 0.001$). Compared with the All 100% condition, lower-amplitude waves occurred in the Horizontal 85% condition ($P < 0.001$, unpaired t-test, $n = 44, 48$) and the Exc and Inh 85% condition ($P < 0.05$, unpaired t-test, $n = 44, 44$), whereas waves were of higher amplitude in the Inh 85% condition ($P < 0.05$, unpaired t-test, $n = 44, 48$). For these conditions, we also examined wave-amplitude distribution, wave slope, and the number of multipeak waves (Figure 11). A 1-way analysis of variance revealed a significant difference between the conditions in the first segment slope ($F_{6,320} = 11.97$, $P < 0.001$). Compared with the All 100% condition, we found that the first-segment slope was significantly decreased in the Horizontal 85% condition ($P < 0.001$, unpaired t-test, $n = 44, 48$). A 1-way analysis of variance also revealed a significant difference between the conditions in the second-segment slope ($F_{6,320} = 12.88$, $P < 0.001$). Compared with the All 100% condition, we found that the second-segment slope was significantly decreased in the Horizontal 85% condition ($P < 0.01$, unpaired t-test, $n = 44, 48$) and increased in the Inh 85% condition ($P < 0.05$, unpaired t-test, $n = 44, 48$). Thus, of the connection subsets we examined, wave parameters were changed most by a decrease in the strength of all excitatory cortical connections and showed a large change following a decrease in just the strength of intralayer excitatory connections. Decreasing the strength of inhibitory cortical connections produced a change in wave parameters in the opposite direction of a change in excitatory cortical connections.

DISCUSSION

In this study, we used a large-scale model of the thalamocortical system to examine the influence of synaptic strength on SWA and slow-wave morphology. As shown previously, the model integrates detailed neuronal properties with thalamocortical anatomy, corresponding to several square millimeters of visual cortex, to reproduce sleep activity patterns at multiple levels, from intracellular membrane potentials to LFPs.⁸ Simulations were performed using hybrid integrate-and-fire neurons with Hodgkin-Huxley-style³² subthreshold dynamics. Due to the focus on investigating homeostatic aspects of slow-wave regulation for our present purposes, no explicit provisions were made for investigating other aspects of sleep, such as sleep spindles. The results presented here dem-

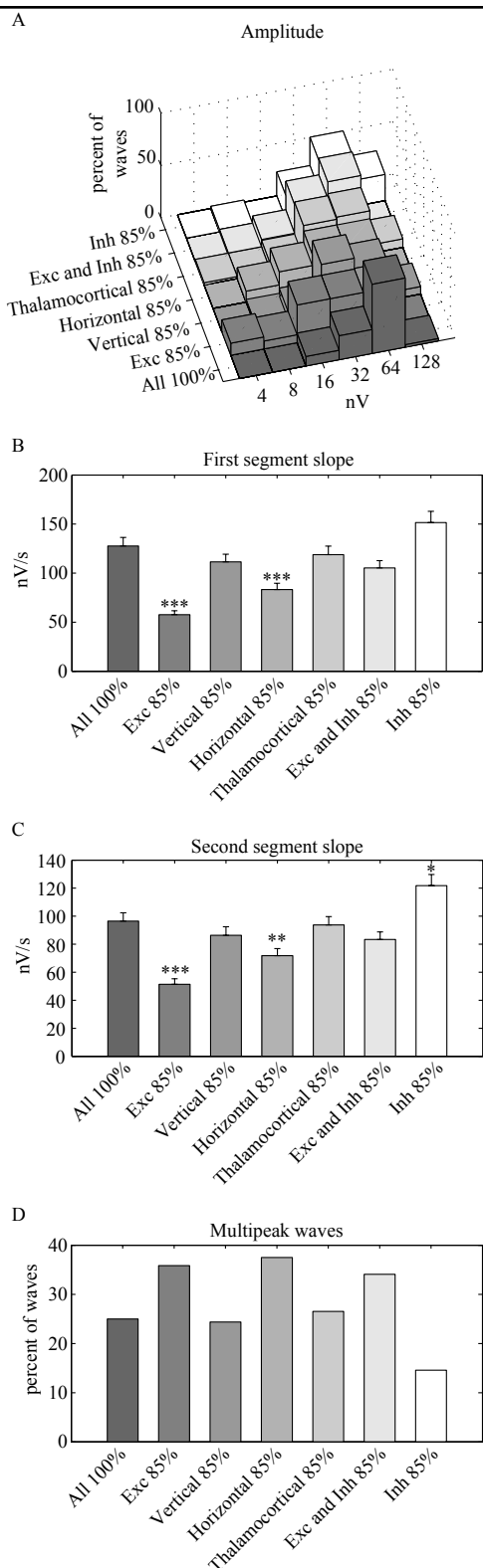


Figure 11—Wave parameters with all connections at 100% strength or with specific sets of connections at 85% strength. **A.** Distribution of slow-wave amplitude, with bin widths increasing in a logarithmic fashion. **B.** Absolute value of the slope of the first segment of the slow waves. **C.** Absolute value of the slope of the second segment of the slow waves. For both B and C, t-tests were performed testing the difference between slopes from the baseline condition and slopes from each of the other conditions. Significance is indicated by asterisks (* $P < 0.05$; ** $P < 0.01$; *** $P < 0.001$). To facilitate comparisons, absolute slope values are shown. **D.** Number of multipeak waves. Exc refers to excitatory; Inh, inhibitory.

onstrate that a reduction in the strength of excitatory corticocortical connections is sufficient to produce a marked decrease in sleep SWA. Moreover, the decrease in SWA is associated with characteristic changes in several slow-wave parameters, including a decreased incidence of high-amplitude waves, a reduced slope of the waves, and an increased occurrence of multiple-wave peaks. The simulations also show that the effects of synaptic strength on these wave parameters are mediated by changes in the amplitude of single-cell oscillations, in the dynamics of network synchronization, and in the rate of neuronal recruitment and decruitment.

As shown in Vyazovskiy et al, (this issue)¹¹ the most important determinant of power in the SWA band is the number of high-amplitude slow oscillations. According to the present simulations, the reduced incidence of high-amplitude waves in the low-synaptic-strength condition was caused by 2 contributing factors: (1) a reduced amplitude of single-cell membrane-potential oscillations due to reduced excitatory postsynaptic potential size and (2) their reduced synchronization across the network due to reduced neuronal coupling. Specifically, the simulations showed that reduced membrane potential oscillations produced less depolarized up states across cortex and, thus, a reduced level of firing in the network. Decreased firing in the network led in turn to a reduced amplitude of oscillations in the LFP. At the same time, decreased synchrony in the network resulted in more cells with oscillations that were out of phase with each other. This resulted in an increased number of up states and down states that effectively canceled each other out, reducing the amplitude of slow waves observed in the LFP. It is worth noting that, even in the high-synaptic-strength condition, neural synchrony was less than in the strongly coupled 50-neuron model presented in Figure 3. This is not surprising for a system as complicated as the thalamocortical system, which includes sparsely connected, bistable units rather than simple coupled oscillators. At the cortical level, the relative synchronization observed during slow-wave sleep is likely the result of the high interconnectivity of the thalamocortical system.

Of particular interest is the observed decrease in the slope of sleep slow waves in the low-synaptic-strength condition. The slope of evoked potentials has traditionally been used as a measure of synaptic strength, notably in studies of long-term potentiation and depression.^{34,35} Usually, the slope is measured on waves induced by electrical stimulation of afferent fibers, but it is likely that the slope of waves generated by spontaneous volleys of activity traveling within the cortex³⁶ also reflects synaptic strength, especially in the case of the high-amplitude waves of NREM sleep. The slope of both the first and the second segment of sleep slow waves was reduced in the simulated low-synaptic-strength condition. Changes of slope are of particular interest because, although they cannot be used to distinguish whether wave period or amplitude might also be changing, the slope is directly influenced by synaptic strength, as demonstrated by the model. The EEG and LFP waves reflect synchronous synaptic activity among large populations of neurons.²⁸ The slope of EEG and LFP waves is a function of the rate of change of synaptic currents,³⁷ which in turn is determined by the change in the rate of firing in the network. The change in the rate of firing is high if neurons are recruited or decruited rapidly and low if neurons are recruited or decruited slowly. The rate of recruitment is, as shown in the model, directly affected by synaptic strength because, the stronger synapses are, the more synaptic current will be added to the network each time a neuron is recruited, leading to more rapid recruitment of other

neurons. Synaptic strength also directly affects the rate of decruitment because, the stronger synapses are, the more synaptic current will be removed from the network each time a neuron is decruited and the more rapidly other neurons will be decruited. Thus, by affecting recruitment and decruitment rates, synaptic strength has a direct influence on wave slope.

Multipeak waves were also more frequent in the low-synaptic-strength condition. In the simulations, multiple peaks were observed when local populations of neurons became hyperpolarized independently of other neural populations. This was more common in the low-synaptic-strength condition, due to the lower rate of decruitment and decreased network synchronization. Intriguingly, using high-density EEG recordings in humans,¹² it was found that when 2 or more slow waves are generated in short order at distant scalp locations, they can converge to produce a single EEG wave with multiple peaks at intermediate locations. Thus, although the multipeak waves modeled here at the level of local circuits occur at vastly different scales compared with the multipeak waves recorded macroscopically with the EEG, it appears that, at both levels, distinct peaks are often due to the recruitment of distinct populations of neurons.

In this paper, we assume that the strength of excitatory corticocortical connections decreases over the course of sleep, reflecting mechanisms such as a reduction in postsynaptic-receptor number that would lead to reduced excitatory postsynaptic currents. Recent work has demonstrated that a net potentiation of excitatory synapses occurs over the course of wakefulness³⁸ and would thus require downscaling over the course of sleep according to the synaptic homeostasis hypothesis.^{4, 5} However, there is little evidence indicating whether or not inhibitory synapses in adult cortex undergo a net potentiation over the course of wakefulness. It is also unclear what specific sets of excitatory connections are progressively potentiated over the course of wakefulness. We therefore performed further simulations to explore the effect of a decrease in the synaptic strength of inhibitory connections or specific sets of excitatory connections. We found that reducing the strength of interlayer excitatory and thalamocortical connections resulted in a modest decrease in wave parameters from baseline levels that did not reach significance. Reducing the strength of intralayer excitatory connections had a large influence on wave parameters, suggesting that these connections are particularly important to network synchronization. Reducing both excitatory and inhibitory synaptic strength resulted in a decrease of wave amplitude from baseline levels, which leaves open the possibility that inhibitory synapses may be downscaled along with excitatory connections during sleep. A reduction of just cortical inhibitory connection strength resulted in larger waves with steeper slope, indicating that a bias toward excitation results in larger slow waves.

Altogether, the simulations presented here demonstrate that a reduction in synaptic strength is sufficient to explain the decrease in SWA observed over the course of sleep. However, it is important to emphasize that other mechanisms could also lead to changes in SWA. For example, arousal-promoting neuromodulators, the decline of which during the transition from waking to deep sleep is essential for permitting the emergence of sleep slow waves, might conceivably rise back toward levels approaching waking over the course of sleep. To examine this possibility, we simulated sleep under conditions of elevated arousal-promoting neuromodulators and found that changes to slow waves caused by

decreased synaptic strength can be distinguished from changes caused by increased arousal-promoting neuromodulators. Specifically, reducing synaptic strength and increasing arousal-promoting neuromodulators in the model both decreased SWA and slow-wave amplitude and slope. However, when waves of the same amplitude produced by these 2 manipulations were compared, we found that a reduction in synaptic strength resulted in waves with lower slope. This finding is particularly interesting in light of findings from a companion paper examining sleep in humans.¹² Presumably, arousal-promoting neuromodulator levels decrease with increasing sleep depth. We assume here that synaptic strength declines with sleep. In the companion paper, we compared waves from the beginning of the first sleep cycle (when synaptic strength would be high and arousal-promoting neuromodulatory levels would be low) with waves from the middle of the fourth sleep cycle (when synaptic strength would be low and arousal-promoting neuromodulatory levels would be high). As in the simulations, waves of the same amplitude had lower slopes if produced under the conditions we propose have lower synaptic strength than if produced under conditions of presumed increased neuromodulatory levels.

The results of the present simulations, demonstrating that a reduction in the strength of corticocortical synapses leads to a decrease in sleep SWA, as well as to characteristic changes in slow-wave morphology, become especially relevant in the context of 2 companion papers, 1 in rats¹¹ and 1 in humans,¹² that were explicitly aimed at testing the model's predictions. Specifically, in both rat LFP recordings and human EEG recordings, the well-established decrease in sleep SWA between early and late sleep was accompanied by a decrease in the occurrence of high-amplitude slow waves, a reduction in the slope of slow waves, and an increased incidence of multipeak waves. Because these changes in wave morphology closely mirror those observed in the model, they suggest that a key factor underlying the decrease in SWA over the course of sleep may indeed be the reduction of cortical synaptic strength. As has been recently suggested, synaptic strength may be progressively depressed during NREM sleep due to the repeated alternation between activated up states and hyperpolarized down states at around 1 Hz.^{4, 5} Indeed, *in vitro* studies³⁹ and preliminary results from computer simulations (Esser et al, unpublished results) suggest that spike timing-dependent plasticity⁴⁰ may be a mechanism sufficient to produce a generalized downscaling of synapses throughout cortex.

ACKNOWLEDGMENTS

We thank Brady Riedner, Chiara Cirelli and Vladyslav Vyazovskiy for helpful discussions. Supported by NRSA F31 NS55553 to SKE and the NIH Director's Pioneer Award to GT.

REFERENCES

1. Achermann P, Borbely AA. Mathematical models of sleep regulation. *Front Biosci* 2003;8:s683-93.
2. Borbely AA. A two process model of sleep regulation. *Hum Neurobiol* 1982; 1(3):195-204.
3. Daan S, Beersma DG, Borbely AA. Timing of human sleep: recovery process gated by a circadian pacemaker. *Am J Physiol* 1984; 246(2 Pt 2):R161-83.
4. Tononi G, Cirelli C. Sleep function and synaptic homeostasis. *Sleep Med Rev* 2006; 10(1):49-62.

5. Tononi G, Cirelli C. Sleep and synaptic homeostasis: a hypothesis. *Brain Res Bull* 2003;62(2):143-50.
6. Huber R, Ghilardi MF, Massimini M, Tononi G. Local sleep and learning. *Nature* 2004;430(6995):78-81.
7. Huber R, Ghilardi MF, Massimini M, et al. Arm immobilization causes cortical plastic changes and locally decreases sleep slow wave activity. *Nat Neurosci* 2006;9(9):1169-76.
8. Hill S, Tononi G. Modeling sleep and wakefulness in the thalamo-cortical system. *J Neurophysiol* 2005;93(3):1671-98.
9. Steriade M. The corticothalamic system in sleep. *Front Biosci* 2003;8:d878-99.
10. Steriade M, Nunez A, Amzica F. A novel slow (< 1 Hz) oscillation of neocortical neurons in vivo: depolarizing and hyperpolarizing components. *J Neurosci* 1993;13(8):3252-65.
11. Vyazovskiy VV, Riedner BA, Cirelli C, Tononi G. Sleep homeostasis and cortical synchronization: II. A local field potential study of sleep slow waves in the rat. *Sleep* 2007;30:1631-42.
12. Riedner BA, Vyazovskiy VV, Huber R, et al. Sleep homeostasis and cortical synchronization: III. A high-density EEG study of sleep slow waves in the humans. *Sleep* 2007;30:1643-57.
13. Mountcastle VB. The columnar organization of the neocortex. *Brain* 1997;120 (Pt 4):701-22.
14. Van Essen DC, Anderson CH, Felleman DJ. Information processing in the primate visual system: an integrated systems perspective. *Science* 1992;255(5043):419-23.
15. Felleman DJ, Van Essen DC. Distributed hierarchical processing in the primate cerebral cortex. *Cereb Cortex* 1991;1(1):1-47.
16. Sherman SM, Guillery RW. Exploring the thalamus. San Diego: Academic Press, 2001.
17. White EL, Keller A. Cortical circuits : synaptic organization of the cerebral cortex--structure, function, and theory. Boston: Birkhäuser, 1989.
18. Zucker RS, Regehr WG. Short-term synaptic plasticity. *Annu Rev Physiol* 2002;64:355-405.
19. Abbott LF, Varela JA, Sen K, Nelson SB. Synaptic depression and cortical gain control. *Science* 1997;275(5297):220-4.
20. Huguenard JR, McCormick DA. Simulation of the currents involved in rhythmic oscillations in thalamic relay neurons. *J Neurophysiol* 1992;68(4):1373-83.
21. McCormick DA, Bal T. Sleep And Arousal: Thalamocortical Mechanisms. *Annu. Rev. Neurosci* 1997;20:185-215.
22. Huguenard JR, Prince DA. A Novel T-type Current Underlies Prolonged Ca²⁺-dependent Burst firing in GABAergic Neurons of Rat Thalamic Reticular Nucleus. *J Neurosci* 1992;12(10):3804-17.
23. Sanchez-Vives MV, McCormick DA. Cellular and network mechanisms of rhythmic recurrent activity in neocortex. *Nat Neurosci* 2000;3(10):1027-34.
24. Steriade M, Timofeev I, Grenier F. Natural waking and sleep states: a view from inside neocortical neurons. *J Neurophysiol* 2001;85(5):1969-85.
25. McCormick DA. Neurotransmitter Actions in the Thalamus and Cerebral Cortex and their Role in Neuromodulation of Thalamocortical Activity. *Prog Neurobiol* 1992;39:337-388.
26. Vautrin J, Barker JL. Presynaptic quantal plasticity: Katz's original hypothesis revisited. *Synapse* 2003;47(3):184-99.
27. Timofeev I, Grenier F, Bazhenov M, et al. Origin of slow cortical oscillations in deafferented cortical slabs. *Cereb Cortex* 2000;10(12):1185-99.
28. Nunez PL, Srinivasan R. Electric fields of the brain : the neurophysics of EEG. 2nd ed. Oxford ; New York: Oxford University Press, 2006.
29. Niedermeyer E, Lopes da Silva FH. Electroencephalography, basic principles, clinical applications, and related fields. 4th ed. Baltimore: Williams & Wilkins, 1999.
30. Rosenblum MG, Pikovsky AS, Kurths J. Phase synchronization of chaotic oscillators. *Physical Review Letters* 1996;76(11):1804-1807.
31. Mardia KV. Statistics of directional data. London, New York,: Academic Press, 1972.
32. Hodgkin AL, Huxley AF. A quantitative description of membrane current and its application to conduction and excitation in nerve. *J Physiol* 1952;117(4):500-44.
33. Pikovsky A, Rosenblum M, Kurths J. Synchronization : a universal concept in nonlinear sciences. Cambridge: Cambridge University Press, 2001.
34. Glazewski S, Herman C, McKenna M, et al. Long-term potentiation in vivo in layers II/III of rat barrel cortex. *Neuropharmacology* 1998;37(4-5):581-92.
35. O'Boyle MP, Do V, Derrick BE, Claiborne BJ. In vivo recordings of long-term potentiation and long-term depression in the dentate gyrus of the neonatal rat. *J Neurophysiol* 2004;91(2):613-22.
36. Massimini M, Huber R, Ferrarelli F, et al. The sleep slow oscillation as a traveling wave. *J Neurosci* 2004;24(31):6862-70.
37. Rall W. Distinguishing theoretical synaptic potentials computed for different soma-dendritic distributions of synaptic input. *J Neurophysiol* 1967;30(5):1138-68.
38. Pfister-Genskow M, Cirelli C, Tononi G. Molecular evidence for synaptic potentiation during waking and synaptic downscaling during sleep *Sleep* 2007;30(Abstract Supplement):A5-A6.
39. Czarnecki A, Birtoli B, Ulrich D. Cellular mechanisms of burst-firing mediated long-term depression in rat neocortical pyramidal cells. *J Physiol* 2007;578(2):471-9.
40. Markram H, Lubke J, Frotscher M, Sakmann B. Regulation of synaptic efficacy by coincidence of postsynaptic APs and EPSPs. *Science* 1997;275(5297):213-5.